Cloud fraction determined by thermal infrared and visible all-sky cameras

Christine Aebi[1,2], Julian Gröbner[1], and Niklaus Kämpfer[2]

[1]Physikalisch-Meteorologisches Observatorium Davos, World Radiation Center, Davos, Switzerland.
[2]Oeschger Center for Climate Change Research and Institute of Applied Physics, University of Bern, Bern, Switzerland.

Correspondence to: Aebi Christine (christine.aebi@pmodwrc.ch)

Abstract. The thermal infrared cloud camera (IRCCAM) is a prototype instrument that determines cloud fraction continuously during day and nighttime with high temporal resolution. It has been developed and tested at Physikalisch-Meteorologisches Observatorium Davos/World Radiation Center (PMOD/WRC) in Davos, Switzerland. The IRCCAM consists of a commercial microbolometer camera sensitive in the 8 μm - 14 μm wavelength range. Over a time period of two years, the fractional cloud coverage obtained by the IRCCAM is compared with two other commercial cameras sensitive in the visible spectrum (Mobotix Q24M and Schreder VIS-J1006) as well as with the automated partial cloud amount detection algorithm (APCADA) using pyrgeometer data. In comparison to the visible cloud detection algorithms, the IRCCAM shows median difference values of 0.01 to 0.07 cloud fraction wherein around 90 % of the data are within ±0.25 (±2 oktas) cloud fraction. Thus there is no significant difference in the cloud fraction determination of the IRCCAM in comparison to the other study instruments. Analysis indicates no significant difference in the performance of the IRCCAM during day or nighttime and also not in different seasons. The cloud types where all algorithms are in closest agreement are low-level clouds (with median differences in cloud fraction of -0.01 to 0.02), followed by mid-level (0.00) and high-level clouds (-0.13).

1 Introduction

Clouds affect the surface radiation budget and thus the climate system on a local as well as on a global scale. Clouds have an influence on solar and on terrestrial radiation by absorbing, scattering and emitting radiation. The Intergovernmental Panel on Climate Change (IPCC) states that clouds in general and aerosol-cloud interactions in particular generate considerable uncertainty in climate predictions and climate models (IPCC, 2013). Information about cloud coverage is of importance not only in climate topics, but also in the production of electricity, because coverage of the sun with clouds leads to a reduction of energy production from photovoltaic panels (Parida et al., 2011).

The most common practice globally to determine cloud coverage, cloud base height (CBH) and cloud type is human observation (CIMO, 2014). These long-term series of cloud data allow climate studies to be conducted. Cloud detection by human observers has the advantage that the observations are carried out several times per day over a long time period and that it is independent of any technical failure. However, there is no reference standard for human observers and thus the cloud determination is not objective (Boers et al., 2010). Other disadvantages of human observers are that the temporal resolution is coarse

and nighttime determinations are difficult. Since clouds are highly variable in space and time, measurements at high spatial and temporal resolution with small measurement uncertainties are needed. Research in the recent past has therefore been conducted in order to find an automated cloud detection instrument (or a combination of such) to replace human observers (Boers et al., 2010; Tapakis and Charalambides, 2013).

5   One alternative to synoptic human observations is to detect clouds with satellites. With a time resolution of 15 minutes, Meteosat Second Generation (MSG) geostationary satellites are able to detect cloud coverage with a higher time resolution than it is accomplished by human observers (Ricciardelli et al., 2010; Werkmeister et al., 2015). Additionally, satellites cover a larger area than ground-based instruments and global coverage of cloud information is possible. However, due to the large field of view (FOV) of satellites, small clouds can be overlooked and thin clouds cannot be distinguished from land (Dybbroe et al.,

10   2005; Calbo and Sabburg, 2008; Heinle et al., 2010). Furthermore, satellites collect information mainly from the highest cloud layer rather than the lower cloud layer closer to the Earth's surface. In order to retrieve information about the lower cloud levels, measurements from the ground are required.

In general, three ground-based cloud measurement techniques are distinguished: radiometers, active column instruments and hemispherical sky cameras. Radiometers measure the incident radiation in different wavelength ranges. In the presence of

15   clouds, depending on the wavelength range, the radiation measured at ground level is lower or higher than without clouds (e.g. Calbo et al., 2001; Mateos Villàn et al., 2010). The FOV of some of these radiometers is rather small. Some of these instruments, such as for example the infrared pyrometer CIR-7 (Nephelo) (Tapakis and Charalambides, 2013) or Nubiscope (Boers et al., 2010; Feister et al., 2010), measure in the 8 μm - 14 μm wavelength range of the spectrum. In order to retrieve cloud information of the whole upper hemisphere, Nephelo consists of seven radiometers which scan the sky. The Nubiscope

20   consists of one radiometer only, which scans the whole upper hemisphere. Such a scan takes several minutes, which is a limitation on the retrieval of cloud fraction information when for example fast-moving clouds occur (Berger et al., 2005). In general, these instruments give information about cloud fraction for three different levels, cloud types and cloud base height (CBH) (Wauben, 2006). Brocard et al. (2011) presents a method using data from the tropospheric water vapour radiometer (TROWARA) to determine cirrus clouds from the measured fluctuations in the sky infrared brightness temperature.

25   The active cloud measurement instruments send a laser pulse to the sky and measure the reflected photons. The photons are scattered back by hydrometeors in clouds and, depending on the time and the amount of reflected photons measured, the cloud base height can be determined. However, the laser pulse is not only scattered by cloud hydrometeors, but also by aerosols (Liu et al., 2015). Examples of active remote sensing instruments are radars (Kato et al., 2001; Feister et al., 2010), lidars (Campbell et al., 2002; Zhao et al., 2014) and ceilometers (Martucci et al., 2010). The disadvantage of these measurements is

30   the lack of information about the whole sky. Thus, with for example ceilometers, a fully covered or cloud-free sky is detected with considerable accuracy, however, the detection of oktas 1 to 7 is more difficult (Boers et al., 2010).

The third group of ground-based cloud detection instruments comprises the hemispherical sky cameras, which have a 180° view of the upper hemisphere. The most common all-sky cameras are the total sky imager (TSI) (Long et al., 2006) and the whole sky imager (WSI) (Shields et al., 2013). Whereas the TSI is sensitive in the visible spectrum, the WSI acquires information in

35   seven different spectral ranges in the visible and in the near infrared regions. A special version of the WSI also allows nighttime

measurements (Feister and Shields, 2005). Other cloud research has been undertaken with low-cost commercial cameras (e.g. Calbo and Sabburg, 2008; Cazorla et al., 2008; Kazantzidis et al., 2012; Wacker et al., 2015). All these hemispherical sky cameras operate well during daytime, but give no information during nighttime. Thus, there is increasing interest in deployment of cloud cameras sensitive in the thermal infrared region of the spectrum. Ground-based thermal infrared all-sky cameras have

5   the advantage of delivering continuous information about cloud coverage, cloud base height and cloud type during day and nighttime, which in turn is of interest for climate studies.

The infrared cloud imager (ICI) is a ground-based sky camera sensitive in the 8 μm - 14 μm wavelength range and with a resolution of 320 $\times$ 240 pixels (Shaw et al., 2005; Thurairajah and Shaw, 2005; Smith and Toumi, 2008). The Solmirus all-sky infrared visible analyser (ASIVA) has been presented by Klebe et al. (2014). ASIVA consists of two cameras, one measur-

10   ing in the visible and the other one in the 8 μm - 13 μm wavelength range. The whole-sky infrared cloud measuring system (WSIRCMS) (Liu et al., 2013) is an all-sky cloud camera sensitive in the 8 μm - 14 μm wavelength range, which consists of nine cameras measuring at the zenith and at eight surrounding positions. With a time resolution of 15 minutes, information about cloud cover, CBH and cloud type are determined. This instrument has an accuracy of $\pm$0.3 oktas compared to visual observations (Liu et al., 2013).

15   The current study describes a newly developed instrument, the thermal infrared cloud camera (IRCCAM), that consists of a modified commercial thermal camera that gives information about cloud conditions with a 180° FOV and a time resolution of 1 minute. It measures in the wavelength range of 8 μm - 14 μm. The IRCCAM has been in use at the Physikalisch-Meteorologisches Observatorium Davos/World Radiation Center (PMOD/WRC), Davos, Switzerland, since September 2015 and is measuring continuously day and night. The performance of the IRCCAM regarding cloud fraction is compared with data

20   from two visible all-sky cameras and the automatic partial cloud amount detection algorithm (APCADA) (Dürr and Philipona, 2004). In section 2 the instruments and cloud detection algorithms are presented. The comparison of the calculated cloud fractions based on different instruments and algorithms are analysed and discussed overall and for different times of day, seasons and cloud classes separately in section 3. Section 4 provides a summary and conclusions.

2   Data and Methods

25   All three all-sky camera systems used for the current study are installed at the Physikalisch-Meteorologisches Observatorium Davos/World Radiation Center (PMOD/WRC), Davos, located in the Swiss Alps (46.81°N, 9.84°E, 1,594 m asl). There are two commercial cameras, one from Mobotix AG and the other from Schreder GmbH, both measuring in the visible spectrum, and a newly developed all-sky camera (IRCCAM) sensitive in the infrared wavelength range from 8 μm - 14 μm. The instruments themselves and their respective analysis software are described in the following subsections. Also, the automatic partial cloud

30   amount detection algorithm (APCADA) is briefly described in Section 2.4.

The analysis of the data from the thermal infrared cloud camera (IRCCAM) is performed for the time period September 21, 2015 to September 30, 2017, with a sizeable data gap between December 20, 2016 and February 24, 2017 due to maintenance of the instrument. Mobotix and APCADA data are available for the whole aforementioned time period. Schreder data are

Atmospheric
Measurement
Techniques
Discussions

Open Access

only available since March 9, 2016. Thus the analysis of these data is only performed for the time period March 9, 2016 to September 30, 2017.

2.1 Thermal infrared cloud camera

The Infrared Cloud Camera (IRCCAM) (Figure 1) consists of a commercial thermal infrared camera (Gobi-640-GigE) from Xenics (www.xenics.com). The camera is an uncooled microbolometer sensitive in the wavelength range of 8 μm - 14 μm. The chosen focal length of the camera objective is 25 mm and the field of view $18° \times 24°$. The image resolution is 640×480 pixels. The camera is located on top of a frame looking downward on a gold-plated spherically shaped aluminium mirror such that the entire upper hemisphere is imaged on the camera sensor. The complete system is 1.9 m high and the distance between the camera objective and the mirror is about 1.2 m. These dimensions were chosen in order to reflect the radiation from the whole upper hemisphere onto the mirror and to minimise the area of the sky hidden by the camera itself. The arm holding the camera above the mirror is additionally fixed with two wire ropes to stabilise the camera against wind. The mirror is gold-plated to reduce the emissivity of the mirror and to make measurement of the infrared sky radiation largely insensitive to the mirror temperature. Several temperature probes are included to monitor the mirror, camera and ambient temperatures.

The camera of the IRCCAM was calibrated in the laboratory of PMOD/WRC in order to determine the brightness temperature or the absolute radiance in $Wm^{-2}sr^{-1}$ for every pixel in an IRCCAM image. The absolute calibration was obtained by placing the camera in front of the aperture of a well characterised blackbody at a range of known temperatures between -20 °C and +20 °C in steps of 5 °C (Gröbner, 2008). The radiance emitted by a blackbody radiator can be calculated using the Planck radiation formula,

$$L_\lambda(T) = \frac{2hc^2}{\lambda^5} \frac{1}{e^{\frac{hc}{k\lambda T}} - 1} \tag{1}$$

where T is the temperature, λ the wavelength, h is the Planck constant, 6.6261×10^{-34} Js, c the speed of light, 299'792'458 ms^{-1} and k the Boltzmann constant, 1.3806×10^{-23} J K^{-1}. For the IRCCAM camera, assuming a nominal spectrally flat response between 8 μm and 14 μm, this yields,

$$L_{8-14} = \int\limits_{8}^{14} L_\lambda(T)d\lambda \tag{2}$$

where T is the effective temperature of the blackbody (Gröbner, 2008) and L_{8-14} the integrated radiance measured by the IRCCAM camera. To retrieve the brightness temperature (T_B) from the integrated radiance L_{8-14}, Eq. 2 cannot be solved analytically. Therefore, as an approximation, we are using a polynomial function $T_B = f(L_{8-14})$ to retrieve the brightness temperature T_B from the radiance L_{8-14}. Using Eq. 2, L_{8-14} values are calculated for temperatures in the range of -40 °C and +40 °C assuming a nominal spectrally flat response function of the IRCCAM. The resulting fitting function is a polynomial function third order (see Figure 2), which is thereafter used to retrieve T_B from the integrated radiance L_{8-14} for every pixel in an IRCCAM image.

The IRCCAM calibration in the blackbody aperture was performed on March 16, 2016 and all its images are calibrated with the

corresponding calibration function. The calibration uncertainty of the camera in terms of brightness temperatures (in a range of -40 °C and +40 °C) is estimated at 1 K for a Planck spectrum as emitted by a blackbody radiator. Furthermore, a temperature correction function for the camera was derived from these laboratory calibrations in order to correct the measurements obtained at ambient temperatures outdoors.

5   The hemispherical sky images taken by the IRCCAM are converted to polar coordinates (Θ, Φ) for the purpose of retrieving brightness temperatures in dependence of zenith and azimuth respectively. Due to slight aberrations in the optical system of the IRCCAM, the Θ coordinate does not follow a linear relationship with the sky zenith angle, producing a distorted sky image. Therefore, a correction function was determined by correlating the apparent solar position as measured by the IRCCAM with the true solar position obtained by a solar position algorithm. This correction function was then applied to the raw camera

10   images to obtain undistorted images of the sky hemisphere.

One should note that observing the sun with the Gobi camera implies that the spectral filter used in the camera to limit the spectral sensitivity to the 8 μm - 14 μm wavelength band has some leakage at shorter wavelengths. Fortunately, this leakage is confined to a narrow region around the solar disk as shown in Figure 3. Thus it has no effect on the remaining part of the sky images taken by the IRCCAM during daytime measurements.

15   The main objective of the IRCCAM study is to determine cloud properties from the measured sky radiance distributions. The cloudy pixels in every image are determined from their observed higher radiances with respect to that of a cloud-free sky. The clear sky radiance distributions are determined from radiative transfer calculations using MODTRAN 5.1 (Berk et al., 2005), using as input parameters screen-level air temperature and integrated water vapour (IWV). The temperature was determined at 2 m elevation obtained from a nearby SwissMetNet station, while the IWV was retrieved from GPS signals operated by

20   the Federal Office for Topography and archived in the Studies in Atmospheric Radiation Transfer and Water Vapour Effects (STARTWAVE) database hosted at IAP, Bern (Morland et al., 2006). For practical reasons, a lookup table (LUT) for a range of temperatures and IWV was generated which was then used to compute the reference clear sky radiance distribution for every single image taken by the camera.

The sky brightness temperature distribution as measured on a cloud-free day (June 18, 2017 10:49 UTC) and the corresponding

25   modelled sky brightness temperature are shown in Figure 3a and Figure 3b, respectively. As expected, the lowest radiance is emitted at the zenith, with a gradual increase at increasing zenith angle, until the measured effective sky brightness temperature at the horizon is nearly equal to ambient air temperature (Smith and Toumi, 2008). Figure 3c shows the profiles of the measured and modelled brightness temperatures along one azimuth position going through the solar position (yellow line in Figure 3a). As can be seen in Figure 3c, the measured and modelled sky distributions agree fairly well, with large deviations at high zenith

30   angles due to the mountains obstructing the horizon around Davos. The shortwave leakage from the sun can also be clearly seen around pixel number 180 and a smaller deviation at pixel number 239 from the wires holding the frame of the camera.

The average difference between the measured and modelled clear sky radiance distributions was determined for several clear sky days during the measurement period in order to use that information when retrieving clouds from the IRCCAM images. Such differences can arise on the one hand from the rather crude radiative transfer modelling which uses as input parameters to

35   the model only surface temperature and IWV, and on the other hand from instrumental effects such as calibration uncertainty

of ± 1 K, the effect of the mirror temperature which has not been taken into account, and a possible mismatch between actual and nominal spectral response functions of the IRCCAM camera. The validation measurements span 8 days, with full sky measurements obtained every minute, yielding a total of 11,512 images for the analysis. For every image, the corresponding sky radiance distribution was calculated from the LUT, as shown in Figure 3b. The residuals between the measured and modelled

5   sky radiance distributions were calculated by averaging over all data points with zenith angles smaller than $60°$, while removing the elements of the IRCCAM within the field of view of the camera (frame and wires), resulting in one value per image. The brightness temperature differences between IRCCAM and model calculations show a mean difference of $+4.0$ K and a standard deviation of 2.4 K over the whole time period. The observed variability comes equally from day to day variations as well as variations within a single day. No systematic differences are observed between day and nighttime data.

10   The stability of the camera over the measurement period is investigated by comparing the horizon brightness temperature derived from the IRCCAM with the ambient air temperature measured at the nearby SwissMetNet station. As mentioned by Smith and Toumi (2008), the horizon brightness temperature derived from the IRCCAM should approach the surface air temperature close to the horizon. Indeed, the average difference between the horizon brightness temperature derived from the IRCCAM and the surface air temperature was 0.1 K with a standard deviation of 2.4 K, showing no drifts over the measurement

15   period, confirming the good stability of the IRCCAM during this period. The good agreement of 0.1 K between the derived horizon brightness temperature from the IRCCAM and the surface air temperature confirms the absolute calibration uncertainty of ± 1 K of the IRCCAM. Therefore, the observed discrepancy of 4 K between measurements and model calculations mentioned previously can probably be attributed to the uncertainties in the model parameters used to produce the LUT.

2.1.1   Cloud detection algorithm

20   After setting up the IRCCAM, a horizon mask is created initially to determine the area of the IRCCAM image representing the sky hemisphere. A clear sky image is selected manually, and the sky area is selected by the very low sky brightness temperatures with respect to the local obstructions with much larger brightness temperatures. This image mask contains local obstructions such as the IRCCAM frame as well as the horizon, which in the case of Davos consists of mountains limiting the field of view of the IRCCAM. The total number of pixels within the mask is used as reference and the cloud fraction is defined as the

25   number of pixels detected as cloudy relative to that total number.

The algorithm to determine cloudy pixels from an IRCCAM image consists of two parts. The first part uses the clear sky model calculations as reference to retrieve low to mid-level clouds with a large temperature difference compared to the clear sky reference. In this part of the algorithm, cloudy pixels are defined for sky brightness temperatures greater than the background clear sky values with a threshold value of 6.5 K. A rather large threshold value was chosen to avoid any erroneous clear sky

30   misclassifications as cloudy pixels, therefore leaving thinner and higher clouds with lower brightness temperatures for the second part of the algorithm.

In order to determine the thin and high-level clouds within an IRCCAM image, non cloudy pixels remaining from the first part

Atmospheric
Measurement
Techniques
Discussions

Open Access

of the algorithm are used to fit an empirical clear sky brightness temperature function in dependence on zenith angle,

$$T_B = (T_{65} - a)(\frac{\Theta}{65})^b + a \tag{3}$$

where T_B is the brightness temperature for a given zenith angle Θ, and T_{65}, a and b are the retrieved function parameters (Smith and Toumi, 2008). This second part of the algorithm assumes a smooth variation of the clear sky brightness temper-

5 ature with zenith angle, and thereby determines cloudy pixels as deviations from this smooth function as well as requiring a brightness temperature higher than this empirical clear sky reference. Pixels with a brightness temperature higher than 1.2 K are defined as cloudy and removed from the clear sky data set. This procedure is repeated up to 10 times to iteratively find pixels with a brightness temperature higher than the clear sky function.

One disadvantage of the method is that it requires at least broken cloud conditions, since it does not work well under fully

10 overcast conditions without any clear sky pixels to constrain the fitting procedure. However, apart from high-level cloud conditions such as cirrus clouds, fully overcast conditions are usually detected in the first part of the algorithm due to the higher brightness temperature under these conditions.

The selected threshold of 1.2 K allows detection of low emissivity clouds, but still misses the detection of thin, high-level cirrus clouds even though they can be clearly seen in the IRCCAM images. Unfortunately, reducing the threshold to less than

15 1.2 K results in many clear sky misclassifications as clouds. Therefore under these conditions, it seems that using a spatial smoothness function is not sufficient to infer individual pixels as being cloudy; a more advanced algorithm as discussed in Brocard et al. (2011) is required to define clouds not only on a pixel by pixel basis but as a continuous structure.

Before reaching the final fractional cloud data set, some data filtering procedures are applied: situations with precipitation are removed by considering precipitation measurements from the nearby SwissMetNet station; ice or snow deposition on the

20 IRCCAM mirror is detected by comparing the median radiance of a sky area with the median radiance value of an area on the image showing the frame of the IRCCAM. In cases where the difference between the median values of the two areas is smaller than the empirically defined value of $5\,\mathrm{Wm}^{-2}\mathrm{sr}^{-1}$, the mirror is assumed contaminated by snow or ice and therefore does not reflect the sky, so the image is excluded. The horizon mask does not cover all pixels that do not depict sky, which leads to an offset in the calculated cloud fraction of around 0.04. This offset is removed before comparing the cloud fraction determined

25 by the IRCCAM with other instruments.

2.2 Mobotix camera

A commercial surveillance Q24M camera from Mobotix (www.mobotix.com) has been installed in Davos since 2011. The camera has a fisheye lens and is sensitive in the red-green-blue (RGB) wavelength range. The camera takes images from the

30 whole upper hemisphere with a spatial resolution of 1200×1600 pixels. The camera system is heated, ventilated and installed on a solar tracker with a shading disk. The shading disk avoids overexposed images due to the sun. The time resolution of the Mobotix data is one minute (from sunrise to sunset) and the exposure time is 1/500 s.

An algorithm determines the cloud fraction of each image automatically (Wacker et al., 2015; Aebi et al., 2017). Before ap-

plying the cloud detection algorithm, the images are preprocessed. The distortion of the images is removed by applying a correction function. A horizon mask, which is defined on the basis of a cloud-free image, is applied. After this preprocessing, the colour ratio (the sum of the blue to green ratio plus the blue to red ratio) is calculated per pixel. To perform the cloud determination per pixel, this calculated colour ratio is compared to an empirically defined reference ratio value of 2.2. Com-

5   paring the calculated colour ratio value with this reference value designates whether a pixel is classified as a cloudy pixel or as a cloud-free pixel. The cloud fraction is calculated by the sum of all cloud pixels divided by the total number of sky pixels.

The cloud classes are determined with a slightly adapted algorithm from Heinle et al. (2010) which is based on statistical features (Wacker et al., 2015, Aebi et al., 2017). The cloud classes determined are stratocumulus (Sc), cumulus (Cu), stratus-altostratus (St-As), cumulonimbus-nimbostratus (Cb-Ns), cirrocumulus-altocumulus (Cc-Ac), cirrus-cirrostratus (Ci-Cs) and

10   cloud-free (Cf).

2.3 Schreder camera

The total sky camera J1006 from Schreder GmbH (www.schreder-cms.com) consists of a digital camera with a fisheye lens. The J1006 Schreder camera is sensitive in the RGB region of the spectrum and takes two images every minute with different exposure times (1/500 s and 1/1600 s, respectively). The aperture is fixed at $f/8$ for both images. The resolution of the images

15   is 1200×1600 pixels. The camera comes equipped with a weatherproof housing and a ventilation system.

The images from the Schreder camera are analysed using two different algorithms. The original software is directly delivered from Schreder GmbH. Before calculating the fractional cloud coverage, the images are preprocessed. In a first step, the centre of the image is defined manually. In a second step, the maximum zenith angle of the area taken into account for further analyses is defined. Unfortunately, the maximum possible zenith angle is only 70° and thus a larger fraction of the sky cannot be analysed.

20   After the distortion of the images is removed, in a fourth step a horizon mask is defined on the basis of a cloud-free image. The mask also excludes the pixels around the sun. In a last step, a threshold is defined which specifies whether a pixel is classified as cloud or no cloud. In the following, the term Schreder refers to data where this algorithm is used.

Due to the Schreder algorithm's limitation of a maximum zenith angle of 70°, we applied the same algorithm as the one for the Mobotix camera to the Schreder camera images also (thereafter referred to as Schreder$_{pmod}$). The algorithm Schreder$_{pmod}$

25   has the advantage that the whole upper hemisphere is considered when calculating the fractional cloud coverage. Thus, a new horizon mask is defined on the basis of a cloud-free image and the colour ratio reference to distinguish between clouds and no clouds and assigned an empirical value of 2.5, which is slightly different from the one used for the Mobotix camera. The Schreder camera in Davos has been measuring continuously since March 2016.

2.4 APCADA

30   The automated partial cloud amount detection algorithm (APCADA) determines the cloud amount in oktas using downward longwave radiation from pyrgeometers, temperature and relative humidity measured at screen-level height (Dürr and Philipona, 2004). APCADA is only able to detect low- and mid-level clouds and is not sensitive to high-level clouds. The time resolution of APCADA is 10 minutes during day and nighttime. The agreement of APCADA compared to synoptic observations at

high-altitude and midlatitude stations, such as Davos, is that 82 to 87 % of cases during day and nighttime have a maximum difference of ±1 okta (± 0.125 cloud fraction) and between 90 to 95 % of cases have a difference of ±2 oktas (± 0.25 cloud fraction) (Dürr and Philipona, 2004).

In order to compare the cloud coverage information retrieved from APCADA with the fractional cloud coverages retrieved

5   from the cameras, the okta values are converted to fractional cloud coverage values by multiplying the okta values with 0.125. In the current study, APCADA is mainly used for comparisons of the nighttime data of the IRCCAM.

3   Results

In the aforementioned time period September 21, 2015 to September 30, 2017, the IRCCAM data set comprises cloud cover information from 581,730 images. The Mobotix data set comprises 242,249 images (because only daytime data are available)

10   and the Schreder data set 184,746 images (shorter time period and also only daytime). Figure 4 shows the relative frequencies of cloud cover detection from the different camera systems in okta bins. Zero okta corresponds to a cloud fraction of 0 to 0.05 and 8 oktas to a cloud fraction of 0.95 to 1 (Wacker et al., 2015). One to seven oktas correspond to intermediate bins of 0.125 cloud fraction. Cloud-free (0 okta) and overcast (8 oktas) are the cloud coverages that are most often detected in the aforementioned time period. This behaviour also agrees with the analysis of the occurrence of fractional cloud coverages over a longer

15   time period in Davos discussed in Aebi et al. (2017). All four instruments show a similar relative occurrence of cloud coverages of 2 - 6 oktas. It is noteworthy that the IRCCAM is clearly underestimating the occurrence of 0 oktas in comparison to the cameras measuring in the visible spectrum (by up to 13 %). On the other hand, the relative frequency of the IRCCAM of 1 okta is clearly larger (by up to 10 %) compared to the visible cameras. This can be explained by higher brightness temperatures measured in the vicinity of the horizon which the IRCCAM algorithm determines as clouds. Also, at the other end of the scale,

20   the IRCCAM is detecting slightly larger values of a relative frequency of 7 oktas compared to the visible cameras and slightly lower relative frequencies of a measurement of 8 oktas.

As an example, Figure 5 shows the cloud fraction determined on April 4, 2016, where various cloud types and cloud fractions were present. This day starts with an overcast sky and precipitation and therefore the IRCCAM is measuring fractional cloud coverages of more than 0.98. The cloud layer dissolves until it reaches values of 0.1 at around 6 UTC. At this time the sun rises

25   above the effective horizon and the visible all-sky cameras start to measure shortly thereafter. The cloud classes are determined with the algorithm developed by Wacker et al. (2015) based on Mobotix images. In the early morning, the cloud type present is cumulus. The larger difference of more than 0.1 between the cloud fraction determined by the Schreder algorithm and the other algorithms can be explained after a visual observation of the image: the few clouds that are present are located in close proximity to the horizon and thus in the region of the sky that the Schreder algorithm is not able to analyse. The fractional cloud

30   coverage increases again to values of around 0.8 at 7 UTC. At this time, all four cameras and algorithms determine a similar fractional cloud coverage. Around 8 UTC a first cirrostratus-layer appears which is slightly better detected by the IRCCAM and the Mobotix algorithm than by the two algorithms using the Schreder images. Two hours later, around 10 UTC, the main cloud type present is again cumulus. Low-level clouds are quite precisely detected by all camera systems and thus, in this

Atmospheric
Measurement
Techniques
Discussions

Open Access

EGU

situation, the maximum observed difference is only 0.07. Figure 6a shows exactly this situation as RGB-image taken by the Mobotix camera, and the corresponding classifications as cloudy or non-cloudy pixels determined by the IRCCAM (Figure 6b) and by the Mobotix algorithm (Figure 6c). From 11 UTC onwards the cumulus clouds are found in the vicinity of the horizon and cirrus-cirrostratus closer to the zenith. Because the detection of thin and high-level clouds is difficult for all algorithms,

5 the differences in the determined cloud fractions are variable. Again, the Schreder algorithm is not able to analyse the cloud fraction near the horizon and thus it always detects the smallest fraction compared to the other algorithms. The visible cameras continue measuring until 16:23 UTC when the sun sets and afterwards only data from the IRCCAM are available.

3.1 Visible all-sky cameras

10 Before validating the fractional cloud coverage determined by the IRCCAM algorithm, the fractional cloud coverages, which are determined using the visible all-sky cameras Mobotix and Schreder, are compared among each other to gain a better understanding of their performance. The time period analysed here is March 9, 2016 to September 30, 2017, only daytime data, which corresponds to a data set of 184,746 images. Additionally, the results from the visible all-sky cameras are compared with data retrieved from APCADA. For this comparison, 32,902 and 24,907 Mobotix and Schreder images respectively are

15 considered.

The histograms of the residuals of the difference in the cloud fractions (range between [-1;1]) between the visible all-sky cameras are shown in Figure 7 and the corresponding median and 5th and 95th percentiles are shown in Table 1.

As shown in Table 1, the two algorithms from the Schreder camera as well as APCADA underestimate the cloud fraction determined from Mobotix images, with a maximum median difference of -0.04. Although the median difference in cloud frac-

20 tion between the two Schreder algorithms is 0.00, the distribution tends towards more negative values. This more pronounced underestimation of fractional cloud coverage of the Schreder algorithm might be explained by its smaller fraction of the sky being analysed (Figure 7). The underestimation in the retrieved cloud fraction of the Schreder algorithm for 90 % of the data is even slightly larger in comparison to the cloud fraction determined with the Mobotix algorithm. The spread (shown as 5th and 95th percentiles in Table 1) is greatest for all comparisons of the algorithms from the visible cameras with APCADA. As

25 previously mentioned in Section 2.4, APCADA gives the cloud fraction only in steps of 0.125 cloud fraction, and is thus not as accurate as the cloud fraction determined from the cameras, which might explain the large variability.

In Figure 7 it is shown that the distribution of the residuals between the cloud fraction retrieved from Mobotix versus the cloud fraction retrieved from the two Schreder algorithms (Figure 7a and 7b) are left-skewed, which confirms that the cloud fraction retrieved from the two Schreder algorithms underestimates the cloud fraction retrieved from the Mobotix images.

30 Taking the measurement uncertainty of human observers and also of other cloud detection instruments to be ± 1 okta to ± 2 oktas (Boers et al., 2010), we take this as a baseline uncertainty range to test the performance in the detection of cloud fraction of our visible camera systems. The algorithms for the visible camera systems determine the cloud fraction for 94 - 100% of the data within ± 2 okta (± 0.25) and for 77 - 94 % of the data within ± 1 okta (± 0.125). Comparing the cloud fraction determined from APCADA with the cloud fraction determined from the visible cameras shows that in only 62 - 71 % of the cases is there

an agreement of ± 1 okta (± 0.125) and in 83 - 86 % of data an agreement of ± 2 okta (± 0.25). All these results are further discussed in Section 3.2.3.

3.2 IRCCAM Validation

As described in Section 3.1, in up to 94 % of the data set the visible cameras do agree within ± 2 okta (± 0.25) in the cloud
5 fraction detection, so that they can be used to validate the fractional cloud coverage determined by the IRCCAM. For this comparison, a data set of 242,249 images (Mobotix) and a data set of 184,746 images (Schreder) are available. This comparison is only performed for daytime data of the IRCCAM, because from the visible cameras only daytime data are available.

The residuals and some statistical values of the differences between the IRCCAM and the visible cameras are shown in Figure 8 and Table 2. With a median value of 0.01, there is no significant difference between the cloud fraction determined by the
10 IRCCAM and the cloud fraction determined by the Mobotix camera. The differences between the IRCCAM and the Schreder algorithms are only slightly larger, with median values of 0.04 and 0.07 for Schreder$_{pmod}$ and Schreder respectively. The distributions of the residuals IRCCAM-Schreder and IRCCAM-Schreder$_{pmod}$ are quite symmetrical (Figure 8b and 8c). The distribution of the residuals in cloud fraction IRCCAM-Mobotix is slightly left-skewed. The IRCCAM agrees in up to 77 % of the cases within a difference in cloud fraction of $\pm$ 1 okta and in even up to 93 % of the cases within $\pm$ 2 oktas. Thus, in
15 general, we can conclude that the IRCCAM retrieves cloud fraction values within the uncertainty range of the cloud fraction retrieved from the visible cameras.

3.2.1 Cloud Class Analysis

Although the median difference between the cloud fraction determined with the IRCCAM algorithm and the cloud fraction de-
20 termined with the Mobotix algorithm is not significant, it is interesting to analyse differences in cloud fraction depending on the cloud type. The algorithm developed by Wacker et al. (2015) is used to distinguish six selected cloud classes and cloud-free cases automatically on the basis of the Mobotix images. Figure 9 shows the distribution of the residuals of the cloud fraction of the two aforementioned algorithms for (a) cumulus (low-level; N=37,320), (b) cirrocumulus-altocumulus (mid-level; N=52,097) and (c) cirrus-cirrostratus (high-level; N=10,467). The median value of the difference in cloud fraction between
25 IRCCAM and Mobotix for Cu clouds is 0.02 and therefore statistically not significant. In general, all low-level clouds are detected with a median cloud fraction difference of - 0.01 to 0.02 (Table 3). The IRCCAM and the Mobotix camera observe the mid-level cloud class Cc-Ac with a median agreement of 0.00, but with a slightly asymmetric distribution towards negative values. Considering 90 % of the data set of Cc-Ac clouds, the IRCCAM tends to underestimate the cloud fraction for the mid-level cloud class. The spread in the Cc-Ac data (shown as 5th and 95th percentiles in Table 3) is in general slightly larger than the
30 one for low-level clouds. The median value of the residuals in cloud fraction determined on the basis of IRCCAM images and the ones based on Mobotix images for the high-level cloud class Ci-Cs is, at -0.13, significantly larger in comparison to clouds at lower levels. Thus, although we applied the second part of the algorithm to detect thin, high-level clouds from the IRCCAM images, it still misses a large fraction of the Ci-Cs clouds in comparison to the Mobotix camera. The distribution (Figure 9c)

of the residuals is clearly wider, which leads to 5th and 95th percentiles of -0.42 and 0.21 respectively. Due to the large spread, and also as shown in Aebi et al. (2017), the visible camera systems also have difficulties in detecting the thin, high-level clouds.

3.2.2 Day-night differences

5   So far, only daytime data have been analysed. At PMOD/WRC in Davos, during nighttime the cloud fraction is retrieved from pyrgeometers as well as from the IRCCAM. Therefore the IRCCAM cloud coverage data are compared with the data retrieved from the automated partial cloud amount detection algorithm (APCADA), which uses pyrgeometer data, which calculates cloud fractions independent of the time of day. As explained in Section 2.4, APCADA only determines the cloud fraction from low- to mid-level clouds and gives no information about high-level clouds. It also gives the cloud fraction only in okta-steps
10   (0.125 cloud fraction).

Table 4 shows the median values of the residuals of the cloud fraction between IRCCAM and APCADA for all available data (N=103,635), only daytime data (N=32,902) and only nighttime data (N=70,722) and the corresponding 5th and 95th percentiles separately. The overall median value in cloud fraction between IRCCAM and APCADA is, at 0.05, in a similar range as the ones for the comparison of the cloud fraction determined with the cloud cameras. The median value for daytime data is,
15   at 0.06, only slightly larger than the one for nighttime data (0.04). However, the spread of the residuals is notably broad mainly during nighttime with a large positive 95th percentile value (0.65). However, because APCADA already showed larger spreads in the residuals in comparison to the fractional cloud coverage determined with the visible all-sky cameras, it is not possible to draw the conclusion that the IRCCAM is overestimating the cloud fraction at nighttime.

3.2.3 Seasonal variations

20   The percentage of agreement in the determined cloud fraction between the sky cameras and APCADA separately is given in Table 5. All values above the grey cells designate the fraction of data that agree within ±0.125 (±1 okta) fractional cloud coverage between two individual algorithms and all values below the grey cells indicate the fraction that agree within ±0.25 (±2 oktas).

25   The agreement of the IRCCAM in comparison with different visible all-sky cameras and APCADA is that 59–77 % of the IRCCAM data are within ± 0.125 fractional cloud coverage (±1 okta) and 78 - 93 % of the data are within ±0.25 fractional cloud coverage (±2 oktas) and thus in a similar range as state of the art cloud detection instruments. These values of the IRC-CAM are only slightly lower than the agreement that the visible cameras have among each other. The close agreement between the two algorithms Schreder and Schreder$_{pmod}$ is noteworthy, although they analyse a different number of pixels of the images.

30   The same analysis was also performed with respect to the four seasons to analyse whether there are seasonal variations. The summer and winter values are shown in Table 6. For all algorithms there is a slightly closer agreement in the determined cloud fraction in the winter months in comparison to the summer months. In winter, the IRCCAM agrees with the other cameras in 78 - 83 % of the data within ±0.125 and as high as 84 - 94 % within ±0.25. In summer, the agreement in cloud fraction is only

Atmospheric
Measurement
Techniques
Discussions

54 - 71 % of the data within ±0.125, but nevertheless, 84 - 91 % of values fall within ±0.25. Also the values for spring and autumn are in a similar range as the ones for summer and winter. Thus, the IRCCAM (and also the other camera systems) do not show any significant variation in any of the seasons.

5   **4   Conclusions**

The current study describes a newly developed instrument - the thermal infrared cloud camera (IRCCAM) and its algorithm - to determine cloud fraction on the basis of brightness temperature distributions. The cloud fraction determined on the basis of IRCCAM images is compared with the cloud fraction determined on the basis of images from two different visible camera systems (one analysed with two different algorithms) and with the partial fractional cloud amount determined with APCADA.

10   The overall agreement of the determined cloud fraction from the IRCCAM with the fractional cloud coverage determined from other instruments and algorithms is in the median 0.01 - 0.07 fractional cloud coverage. The IRCCAM has an agreement of ±2 oktas (±0.25) in more than 90 % of cases and an agreement of ±1 okta (±0.125) in up to 77 % of the cases in comparison to other instruments. Thus, in only 10 % of the data, the IRCCAM typically overestimates the cloud fraction in comparison with the cloud fraction determined from the all-sky cameras sensitive in the visible region of the spectrum.

15   In general, there is no significant difference in the performance of the IRCCAM in the different seasons. Analysis of the median values of the residuals between the cloud fraction determined from the IRCCAM with the ones calculated from APCADA shows almost no difference between day and nighttime. However, the spread of the data is larger during nighttime than during daytime.

The differentiation of cloud classes shows that low-level clouds are best detected with all camera systems, followed by mid-

20   level clouds. Although an additional algorithm is applied to detect high-level clouds from the IRCCAM images, they are not yet detected in all cases due to their very low emissivity.

Overall, the IRCCAM is able to determine cloud fraction with a good agreement in comparison to all-sky cameras sensitive in the visible spectrum and with no significant differences in its performance during different times of the day or different seasons. Thus, the IRCCAM is a stable system that can be used 24 hours per day with a high temporal resolution. In comparison to other

25   state of the art cloud detection instruments (e.g. ceilometer or Nubiscope) it has the advantage of depicting the whole upper hemisphere at one specific moment. Its accuracy ranges from similar to rather better than that of the Nubiscope (Feister et al., 2010).

In this study we mainly showed one application of the IRCCAM, which is to retrieve fractional cloud coverage information from the images. However, the known brightness temperature distribution of the sky and thus the known radiance can also be

30   used for other applications such as for example to determine other cloud parameters (cloud type, cloud level) as well as to retrieve information about downward longwave radiation in general. Thus, after some improvements in the hardware (e.g. a heating or ventilation system to avoid a frozen mirror) and software (improvements of the cloud algorithm detecting high-level

Atmospheric
Measurement
Techniques
Discussions

clouds) the IRCCAM might be of interest for a number of further applications.

Atmospheric
Measurement
Techniques
Discussions

References

Aebi, C., Gröbner, J., Kämpfer, N., and Vuilleumier, L.: Cloud radiative effect, cloud fraction and cloud type at two stations in Switzerland using hemispherical sky cameras, Atmospheric Measurement Techniques, 10, 4587–4600, doi:10.5194/amt-10-4587-2017, https://www.atmos-meas-tech.net/10/4587/2017/, 2017.

5 Berger, L., Besnard, T., Genkova, I., Gillotay, D., Long, C., Zanghi, F., Deslondes, J. P., and Perdereau, G.: Image comparison from two cloud cover sensor in infrared and visible spectral regions, in: 21st International Conference on Interactive Information Processing Systems (IIPS) for Meteorology, Oceanography, and Hydrology, 2005.

Berk, A., Anderson, G. P., Acharya, P. K., Bernstein, L. S., Muratov, L., Lee, J., Fox, M. J., Adler-Golden, S. M., Chetwynd, J. H., Hoke, M. L., Lockwood, R. B., Cooley, T. W., and Gardner, J. A.: MODTRAN5: a reformulated atmospheric band model with auxiliary species

10 and practical multiple scattering options, Proc. SPIE, 5655, 88–95, doi:10.1117/12.578758, http://dx.doi.org/10.1117/12.578758, 2005.

Boers, R., de Haij, M. J., Wauben, W. M. F., Baltink, H. K., van Ulft, L. H., Savenije, M., and Long, C. N.: Optimized fractional cloudiness determination from five ground-based remote sensing techniques, Journal of Geophysical Research: Atmospheres, 115, doi:10.1029/2010JD014661, http://dx.doi.org/10.1029/2010JD014661, d24116, 2010.

Brocard, E., Schneebeli, M., and Matzler, C.: Detection of Cirrus Clouds Using Infrared Radiometry, IEEE Transactions on Geoscience and

15 Remote Sensing, 49, 595–602, doi:10.1109/TGRS.2010.2063033, 2011.

Calbo, J. and Sabburg, J.: Feature Extraction from Whole-Sky Ground-Based Images for Cloud-Type Recognition, Journal of Atmospheric and Oceanic Technology, 25, 3–14, doi:10.1175/2007JTECHA959.1, https://doi.org/10.1175/2007JTECHA959.1, 2008.

Calbo, J., Gonzalez, J.-A., and Pagas, D.: A Method for Sky-Condition Classification from Ground-Based Solar Radia-tion Measurements, Journal of Applied Meteorology, 40, 2193–2199, doi:10.1175/1520-0450(2001)040<2193:AMFSCC>2.0.CO;2,

20 https://doi.org/10.1175/1520-0450(2001)040<2193:AMFSCC>2.0.CO;2, 2001.

Campbell, J. R., Hlavka, D. L., Welton, E. J., Flynn, C. J., Turner, D. D., Spinhirne, J. D., III, V. S. S., and Hwang, I. H.: Full-Time, Eye-Safe Cloud and Aerosol Lidar Observation at Atmospheric Radiation Measurement Program Sites: Instruments and Data Pro-cessing, Journal of Atmospheric and Oceanic Technology, 19, 431–442, doi:10.1175/1520-0426(2002)019<0431:FTESCA>2.0.CO;2, https://doi.org/10.1175/1520-0426(2002)019<0431:FTESCA>2.0.CO;2, 2002.

25 Cazorla, A., Olmo, F. J., and Alados-Arboledas, L.: Development of a sky imager for cloud cover assessment, J. Opt. Soc. Am. A, 25, 29–39, doi:10.1364/JOSAA.25.000029, http://josaa.osa.org/abstract.cfm?URI=josaa-25-1-29, 2008.

CIMO: Guide to Meteorological Instruments and Methods of Observation, World Meteorological Organization Bulletin, 8, 2014.

Dürr, B. and Philipona, R.: Automatic cloud amount detection by surface longwave downward radiation measurements, J. Geophys. Res., 109, D05 201, doi:10.1029/2003JD004182, 2004.

30 Dybbroe, A., Karlsson, K.-G., and Thoss, A.: NWCSAF AVHRR Cloud Detection and Analysis Using Dynamic Thresholds and Ra-diative Transfer Modeling. Part I: Algorithm Description, Journal of Applied Meteorology, 44, 39–54, doi:10.1175/JAM-2188.1, https://doi.org/10.1175/JAM-2188.1, 2005.

Feister, U. and Shields, J.: Cloud and radiance measurements with the VIS/NIR Daylight Whole Sky Imager at Lindenberg (Germany), Meteorologische Zeitschrift, 14, 627–639, doi:10.1127/0941-2948/2005/0066, http://dx.doi.org/10.1127/0941-2948/2005/0066, 2005.

35 Feister, U., Möller, H., Sattler, T., Shields, J., Görsdorf, U., and Güldner, J.: Comparison of macroscopic cloud data from ground-based measurements using VIS/NIR and IR instruments at Lindenberg, Germany, Atmospheric Research, 96, 395 – 407,

doi:https://doi.org/10.1016/j.atmosres.2010.01.012, http://www.sciencedirect.com/science/article/pii/S0169809510000232, 15th International Conference on Clouds and Precipitation, 2010.

Gröbner, J.: Operation and investigation of a tilted bottom cavity for pyrgeometer characterizations, Appl. Opt., 47, 4441–4447, doi:10.1364/AO.47.004441, http://ao.osa.org/abstract.cfm?URI=ao-47-24-4441, 2008.

5 Heinle, A., Macke, A., and Srivastav, A.: Automatic cloud classification of whole sky images, Atmos. Meas. Tech., 3, 557–567, doi:10.5194/amt-3-557-2010, 2010.

Kato, S., Mace, G. G., Clothiaux, E. E., Liljegren, J. C., and Austin, R. T.: Doppler Cloud Radar Derived Drop Size Distributions in Liquid Water Stratus Clouds, Journal of the Atmospheric Sciences, 58, 2895–2911, doi:10.1175/1520-0469(2001)058<2895:DCRDDS>2.0.CO;2, https://doi.org/10.1175/1520-0469(2001)058<2895:DCRDDS>2.0.CO;2,
10 2001.

Kazantzidis, A., Tzoumanikas, P., Bais, A. F., Fotopoulos, S., and Economou, G.: Cloud detection and classification with the use of whole-sky ground-based images, Atmos. Res., 113, 80–88, doi:10.1016/j.atmosres.2012.05.005, 2012.

Klebe, D. I., Blatherwick, R. D., and Morris, V. R.: Ground-based all-sky mid-infrared and visible imagery for purposes of characterizing cloud properties, Atmospheric Measurement Techniques, 7, 637–645, doi:10.5194/amt-7-637-2014,
15 https://www.atmos-meas-tech.net/7/637/2014/, 2014.

Liu, L., jin Sun, X., chang Gao, T., and jun Zhao, S.: Comparison of Cloud Properties from Ground-Based Infrared Cloud Measurement and Visual Observations, Journal of Atmospheric and Oceanic Technology, 30, 1171–1179, doi:10.1175/JTECH-D-12-00157.1, https://doi.org/10.1175/JTECH-D-12-00157.1, 2013.

Liu, L., jin Sun, X., chuan Liu, X., chang Gao, T., and jun Zhao, S.: Comparison of Cloud Base Height Derived from a Ground-
20 Based Infrared Cloud Measurement and Two CeilometersAdvances in Meteorology, vol. 2015, Article ID 853861, 8 pages, 2015. doi:10.1155/2015/853861, Advances in Meteorology, 2015, doi:doi:10.1155/2015/853861, 2015.

Long, C. N., Sabburg, J. M., Calbo, J., and Pages, D.: Retrieving cloud characteristics from ground-based daytime color all-sky images, J. Atmos. Oceanic Technol., 23, 633–652, doi:10.1175/JTECH1875.1, 2006.

Martucci, G., Milroy, C., and O'Dowd, C. D.: Detection of Cloud-Base Height Using Jenoptik CHM15K and Vaisala
25 CL31 Ceilometers, Journal of Atmospheric and Oceanic Technology, 27, 305–318, doi:10.1175/2009JTECHA1326.1, https://doi.org/10.1175/2009JTECHA1326.1, 2010.

Mateos Villàn, D., de Miguel Castrillo, A., and Bilbao Santos, J.: Empirical models of UV total radiation and cloud effect study, International Journal of Climatology, 30, 1407–1415, doi:10.1002/joc.1983, http://dx.doi.org/10.1002/joc.1983, 2010.

Morland, J., Deuber, B., Feist, D. G., Martin, L., Nyeki, S., Kämpfer, N., Mätzler, C., Jeannet, P., and Vuilleumier,
30 L.: The STARTWAVE atmospheric water database, Atmos. Chem. Phys., 6, 2039–2056, doi:10.5194/acp-6-2039-2006, http://www.atmos-chem-phys.net/6/2039/2006/, 2006.

Parida, B., Iniyan, S., and Goic, R.: A review of solar photovoltaic technologies, Renewable and Sustainable Energy Reviews, 15, 1625 – 1636, doi:https://doi.org/10.1016/j.rser.2010.11.032, http://www.sciencedirect.com/science/article/pii/S1364032110004016, 2011.

Ricciardelli, E., Romano, F., and Cuomo, V.: A Technique for Classifying Uncertain MOD35/MYD35 Pixels Through Meteosat Second
35 Generation-Spinning Enhanced Visible and Infrared Imager Observations, IEEE Transactions on Geoscience and Remote Sensing, 48, 2137–2149, doi:10.1109/TGRS.2009.2035367, 2010.

Shaw, J. A., Nugent, P. W., Pust, N. J., Thurairajah, B., and Mizutani, K.: Radiometric cloud imaging with an uncooled microbolometer thermal infrared camera, Opt. Express, 13, 5807–5817, doi:10.1364/OPEX.13.005807, http://www.opticsexpress.org/abstract.cfm?URI=oe-13-15-5807, 2005.

Shields, J. E., Karr, M. E., Johnson, R. W., and Burden, A. R.: Day/night whole sky imagers for 24-h cloud and sky assessment: history and

5 overview, Appl. Opt., 52, 1605–1616, doi:10.1364/AO.52.001605, http://ao.osa.org/abstract.cfm?URI=ao-52-8-1605, 2013.

Smith, S. and Toumi, R.: Measuring cloud cover and brightness temperature with a ground-based thermal infrared camera, J. Appl. Meteorol. Climatol., 47, 683–693, doi:10.1175/2007JAMC1615.1, 2008.

Tapakis, R. and Charalambides, A. G.: Equipment and methodologies for cloud detection and classification: A review, Sol. Energy, 95, 392–430, doi:10.1016/j.solener.2012.11.015, 2013.

10 Thurairajah, B. and Shaw, J. A.: Cloud statistics measured with the infrared cloud imager (ICI), IEEE Transactions on Geoscience and Remote Sensing, 43, 2000–2007, doi:10.1109/TGRS.2005.853716, 2005.

Wacker, S., Gröbner, J., Zysset, C., Diener, L., Tzoumanikas, P., Kazantzidis, A., Vuilleumier, L., Stoeckli, R., Nyeki, S., and Kämpfer, N.: Cloud observations in Switzerland using hemispherical sky cameras, J. Geophys. Res., 120, 695–707, doi:10.1002/2014JD022643, 2015.

Wauben, W.: Evaluation of the Nubiscope, Technisch rapport / Koninklijk Nederlands Meteorologisch Instituut, 291, 37., 2006.

15 Werkmeister, A., Lockhoff, M., Schrempf, M., Tohsing, K., Liley, B., and Seckmeyer, G.: Comparing satellite- to ground-based automated and manual cloud coverage observations - a case study, Atmos. Meas. Tech., 8, 2001–2015, doi:10.5194/amt-8-2001-2015, 2015.

Zhao, C., Wang, Y., Wang, Q., Li, Z., Wang, Z., and Liu, D.: A new cloud and aerosol layer detection method based on micropulse lidar measurements, Journal of Geophysical Research: Atmospheres, 119, 6788–6802, doi:10.1002/2014JD021760, http://dx.doi.org/10.1002/2014JD021760, 2014JD021760, 2014.

Figure 1. The Infrared Cloud Camera (IRCCAM) in the measurement enclosure of PMOD/WRC in Davos, Switzerland.
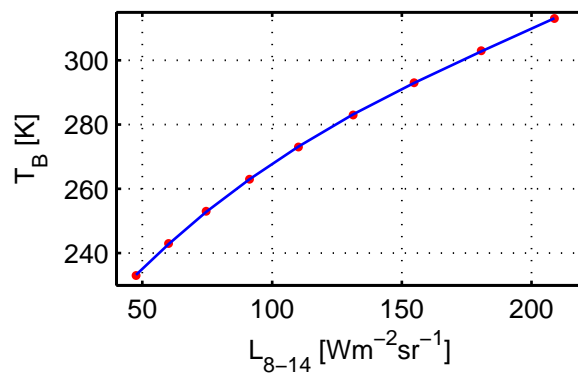
Atmospheric
Measurement
Techniques
Discussions

Open Access

Figure 2. Brightness Temperature T_B versus integrated radiance L_{8-14} for different radiance values (red dots), and the corresponding third order polynomial fitting function (blue line).
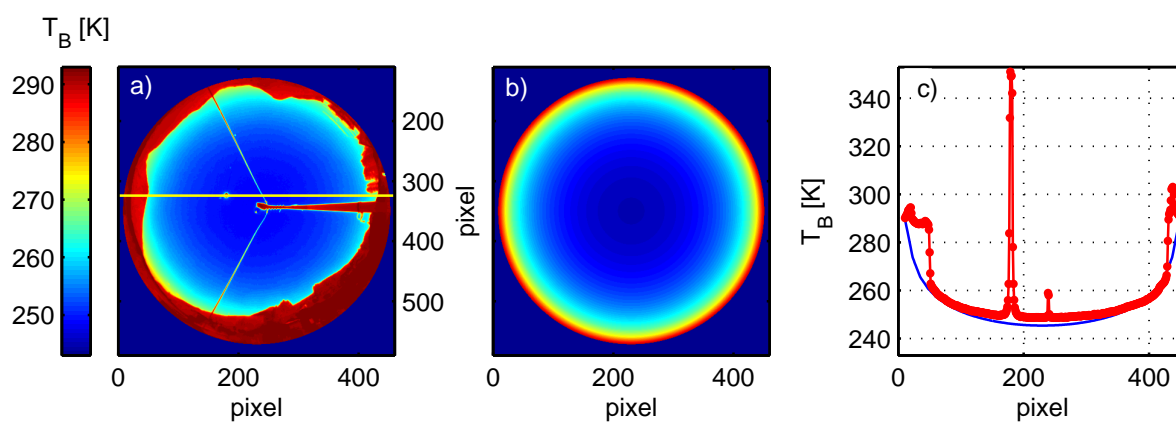
Figure 3. (a) Measured brightness temperature on the cloud-free day June 18, 2017 10:49 UTC (SZA=23 °), (b) the corresponding modelled brightness temperature and (c) the measured (red) and modelled (blue) profile of the sky brightness temperature along one azimuth position (shown as a yellow line in (a)).
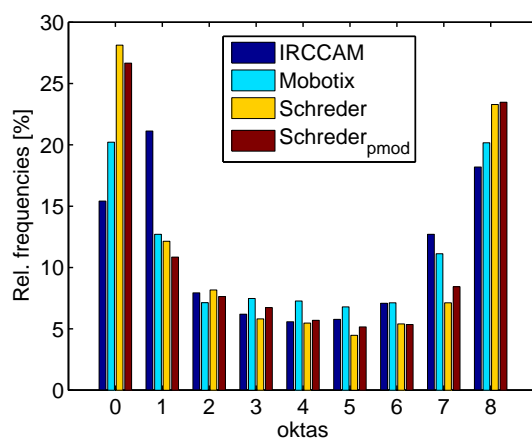
Figure 4. Relative frequencies of the determined cloud coverage of the study instruments for selected bins of cloud coverages at Davos. Zero okta: 0 - 0.050; 1 okta: 0.050 - 0.125; 2 oktas: 0.125 - 0.250; 3 oktas: 0.250 - 0.375; 4 oktas: 0.375 - 0.500; 5 oktas: 0.500 - 0.625; 6 oktas: 0.625 - 0.750; 7 oktas: 0.750 - 0.875; 8 oktas: 0.875 - 1;
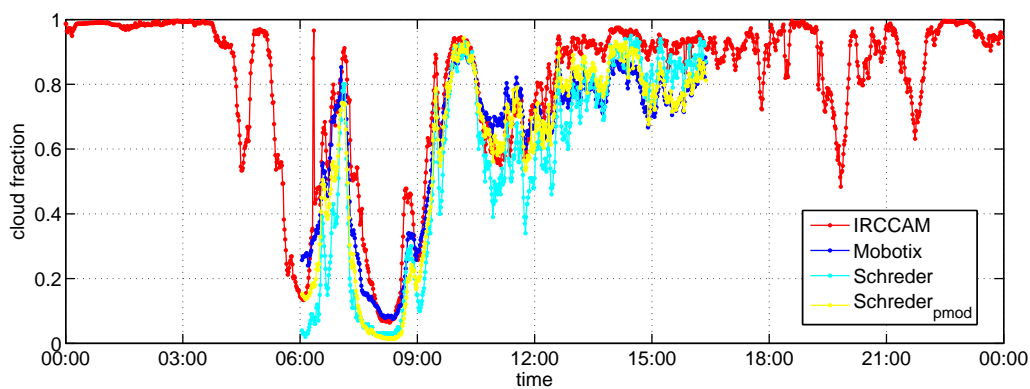
Figure 5. Cloud fraction determined by the study instruments and algorithms (red: IRCCAM, blue: Mobotix, cyan: Schreder, yellow: Schreder_pmod) on April 4, 2016.
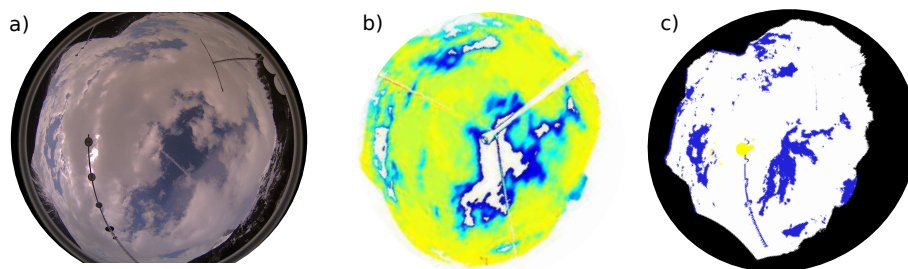
Figure 6. The cloud situation on April 4, 2016 10 UTC on an image from Mobotix (a) and the cloud fraction determined from (b) IRCCAM and (c) Mobotix.
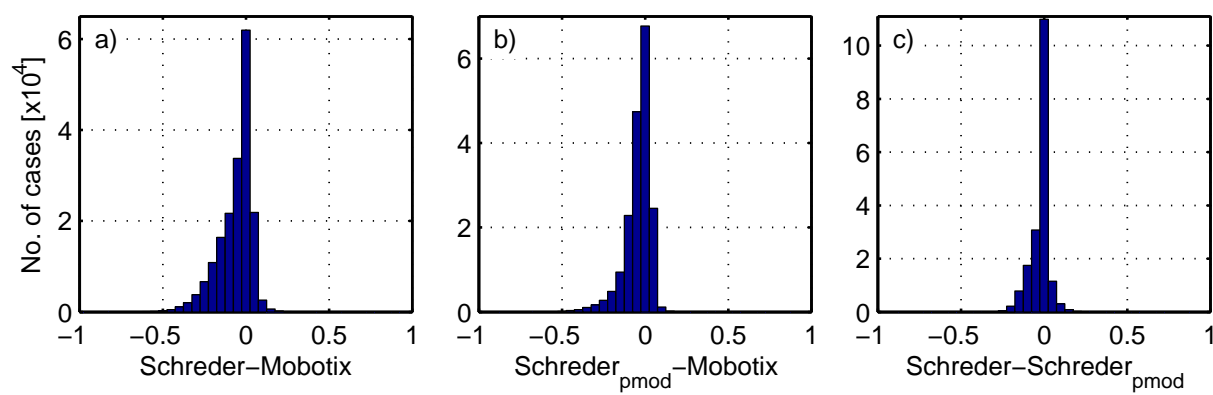
Figure 7. Residuals of the comparison of cloud fraction retrieved from the visible cameras and algorithms used in the study.

Atmospheric
Measurement
Techniques
Discussions

Table 1. Median and 5th and 95th percentiles of the differences in calculated cloud fractions from the visible all-sky cameras and APCADA.
The numbers are in the range [-1;1].

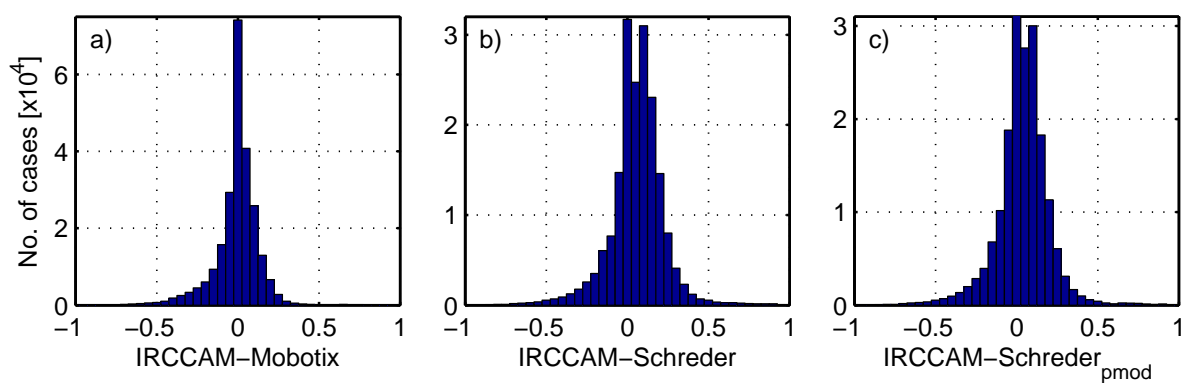|	Cloud fraction		
	median	5th	95th
Schreder - Mobotix	-0.03	-0.26	0.05
Schreder$_{pmod}$ - Mobotix	-0.02	-0.19	0.04
Schreder - Schreder$_{pmod}$	0.00	-0.13	0.04
APCADA - Mobotix	-0.04	-0.43	0.17
APCADA - Schreder	-0.01	-0.38	0.30
APCADA - Schreder$_{pmod}$	-0.01	-0.38	0.26

Figure 8. Residuals of the comparison of cloud fraction retrieved from the IRCCAM versus cloud fraction retrieved from the visible cameras.

Table 2. Median and 5th and 95th percentiles of the differences in calculated cloud fractions between IRCCAM and the visible all-sky cameras.

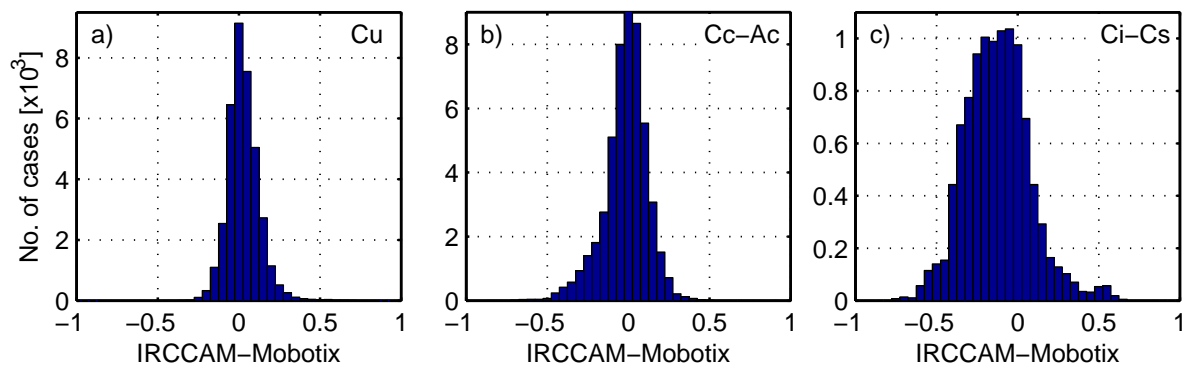|	Cloud fraction		
	median	5th	95th
IRCCAM - Mobotix	0.01	-0.26	0.18
IRCCAM - Schreder	0.07	-0.22	0.29
IRCCAM - Schreder$_{pmod}$	0.04	-0.23	0.26

Figure 9. Residuals of the comparison of cloud fraction determined from IRCCAM images versus cloud fraction determined from Mobotix images for the following cloud classes: Cu: Cumulus, Cc-Ac: Cirrocumulus-Altocumulus, Ci-Cs: Cirrus-Cirrostratus

Atmospheric
Measurement
Techniques
Discussions

Table 3. Median and 5th and 95th percentiles of the differences in calculated cloud fractions from IRCCAM and Mobotix images for selected cloud classes (stratocumulus (Sc), cumulus (Cu), stratus-altostratus (St-As), cumulonimbus-nimbostratus (Cb-Ns), cirrocumulus-altocumulus (Cc-Ac), cirrus-cirrostratus (Ci-Cs) and cloud-free (Cf).

	Cloud fraction		
	median	5th	95th
Sc	0.01	-0.24	0.21
Cu	0.02	-0.12	0.19
St-As	0.00	-0.38	0.11
Cb-Ns	-0.01	-0.22	0.08
Cc-Ac	0.00	-0.27	0.18
Ci-Cs	-0.13	-0.42	0.21
Cf	0.03	-0.03	0.18

Table 4. Median and 5th and 95th percentiles of the differences in calculated cloud fractions from IRCCAM versus APCADA: overall; only daytime and only nighttime.

	Cloud fraction		
	median	5th	95th
IRCCAM - APCADA	0.05	-0.31	0.54
IRCCAM - APCADA day	0.06	-0.18	0.35
IRCCAM - APCADA night	0.04	-0.40	0.65

Table 5. Percentage of fractional cloud coverage data which agree within ± 1 okta (all values above the grey cells) and ± 2 oktas (all values below the grey cells) comparing two algorithms each.

	IRCCAM	Mobotix	Schreder	Schreder$_{pmod}$	APCADA
IRCCAM	-	77%	59%	66%	62%
Mobotix	93%	-	77%	89%	67%
Schreder	88%	94%	-	94%	71%
Schreder$_{pmod}$	90%	97%	100%	-	70%
APCADA	80%	83%	86%	85%	-

Atmospheric
Measurement
Techniques
Discussions

Table 6. Identical to Table 5, but the left values in a cell are for the summer months (June, July, August) and the right values for the winter months (December, January, February).

	IRCCAM	Mobotix	Schreder	Schreder$_{pmod}$	APCADA
IRCCAM	-	71% | 83%	54% | 78%	61% | 80%	62% | 51%
Mobotix	91% | 94%	-	76% | 84%	90% | 87%	66% | 74%
Schreder	89% | 84%	95% | 93%	-	93% | 97%	73% | 89%
Schreder$_{pmod}$	89% | 86%	98% | 95%	100% | 100%	-	71% | 92%
APCADA	87% | 65%	84% | 87%	90% | 97%	88% | 98%	-